Dynamic mechanical properties and σ precipitates strengthen of selective laser melt NiCrFeCoMo_{0.2} high-entropy alloy

Yiyu Huang ^{a,b}, Wenshu Li ^{a,b}, Haoyu Chen ^{a,b}, Qi Wu ^{a,b}, Shaohong Wei ^{a,c}, Bin Liu ^b, Peter K. Liaw ^d, Bingfeng Wang ^{a,b*}

a. School of Materials Science and Engineering, Central South University, Changsha410083, P. R. China;

b. State Key Laboratory of Powder Metallurgy, Central South University, Changsha410083, P. R. China;

c. Dongguan Research Department, Institute of High Energy Physics (IHEP), Chinese Academy of Sciences (CAS), Dongguan 523808, China;

d. Dept Mat Sci & Engn, University of Tennessee, Knoxville, TN 37996 USA.

*Corresponding author.

Tel.: +86 - (731) - 88876244;

E-mail: wangbingfeng@csu.edu.cn (Bingfeng Wang)

Postal address: School of Materials Science and Engineering, Central South University,

Changsha 410083, P. R. China

Abstract

The refractory element σ precipitates can improve the dynamic mechanical properties of selective laser melt (SLM) NiCrFeCoMo_{0.2} high entropy alloy (HEA), to meet the integrated and impact resistance requirements of aerospace and transportation components. The distribution of σ phase in SLM- NiCrFeCoMo_{0.2} HEA can be controlled by micron scale gradient design. In dynamic mechanical tests, the ultimate compressive strength of these specimens is higher than the as-build specimen, reaching 1,970 MPa. Due to the segregation of Mo elements near the molten pool boundary of the as-build SLM-NiCrFeCoMo_{0.2} HEA, more σ precipitates are formed at these locations. In addition, the small angle neutron scattering (SANS) technique was used to analyze the volume fraction of σ precipitation in the specimens.

Key words: Selective laser melt; High-entropy alloy; Micron scale gradient structure design; Dynamic mechanical properties.

1. Introduction

High-entropy alloys (HEAs) with face centered cubic (FCC) structures have excellent mechanical properties, such as a combination of strength, ductility and fracture toughness [1,2]. Selective laser melt (SLM) is a widely studied and used additive manufacturing (AM) method that can produce products with almost full densities [3] and improved mechanical properties [4]. Although the SLM FCC HEAs lose some ductility and gain strengths, compared to conventionally fabricated HEAs [5,6,7], their strength needs to improve engineering applications. Since the NiCrFeCoMo_{0.2} HEA precipitated phases during annealing [8], the study of the σ precipitates strengthening in the SLM-NiCrFeCoMo_{0.2} HEA is indispensable for the application of this alloy in the fields with high requirements for components integrity and impact resistance, such as special ships and aerospace fields.

Due to the super-fast heating and cooling rate (10³ - 108 K/s) of the SLM process [9], resulting in the presence of micron scale composition modulations with excellent mechanical properties [10]. Many researchers promoted the second phase precipitation of SLM-HEAs by heat treatment, and eliminated the defects introduced in the SLM process to improve the strength [11,12]. Jeong et al. [13] reported that the SLM-1%C-CoCrFeMnNi HEA samples annealed at 800 °C still maintained a high dislocation density and could also effectively impede the grain growth due to the presence of nanoscale Cr₂₃C₆ carbides produced by annealing. The grain and sub-grain changes after annealing of SLM alloys have been carefully studied by many researchers [14,15].

However, as the characteristic structure of SLM finished products, the molten pool boundary is often related to the segregation, texture and grain size, but it is often ignored in the study of the SLM-HEAs after heat treatments.

As an method for strengthening alloys, secoend phase strengthening is considering as an effective way to improve the strengths of FCC HEAs precipitated particles prevent dislocation movement in the matrix, sacrifice part of the plasticity and improve strength [16, 17]. There are studies on precipitation enhanced FCC HEAs. For example, Li et al. [18] investigate the dynamic mechanical properties of a series of the CoCrNiMo_x alloys, and the σ precipitates was found in CoCrNiMo_{0.1} and CoCrNiMo_{0.2}. As a result, their dynamic compressive yield strengths were increased about 35.5% and 77.8%, respectively, compared with alloys without the Mo element. Besides, some studies believe that the precipitated phase is inseparable from the high strain hardening rate, which can prevent crack propagation and thus show high plasticity [19]. Also, precipitation formed by refractory elements can hinder grain growth during annealing [20].

In the present work, the micron-scale gradient structure of SLM-NiCrFeCoMo $_{0.2}$ HEA was regulated, and then their mechanical properties were tested with the split-Hopkinson pressure bar (SHPB). Two kinds of refractory σ precipitates with different morphologies were observed, and the blocky σ precipitates may come from the growth of original σ precipitates near the molten pool boundary in the as-built state. In addition, the volume fraction of σ precipitates is determined by the small angle neutron scattering

(SANS) technique. According to the two different forms of σ precipitates, the strength of the precipitates strengthening contribution is calculated.

2. Materials and Methods

The raw materials of the NiCrFeCoMo_{0.2} HEA powder used in the SLM process were high-purity (99.9 at. %) Fe, Co, Ni, Cr, and Mo powders, and they were melted in an induction heating vacuum furnace and then filled into the atomization chamber. The particle size of the powder in the range of $40 \sim 90 \, \mu m$, and the average particle size of the is $67.1 \, \mu m$. The instrument used for SLM was the FS301M (Farsoon Technologies, P. R. China). Argon gas was used as the shielding gas during the SLM process and controlled oxygen content below 300 ppm. The laser power, scanning speed, scanning spacing and powder layer thickness were set to 330 W, 1200 mm/s, 0.1 mm, and 0.06 mm, respectively. On the stainless-steel substrate, rectangular parallelepipeds with a length, width, and height of 500, 10, and 10 mm were printed. After the completion, they were divided into cylindrical samples with a height of 7.2 mm and a diameter of 6 mm. Figure 1 is a schematic diagram of the sample and its relationship with the build direction and shows the direction of the dynamic compression deformation.

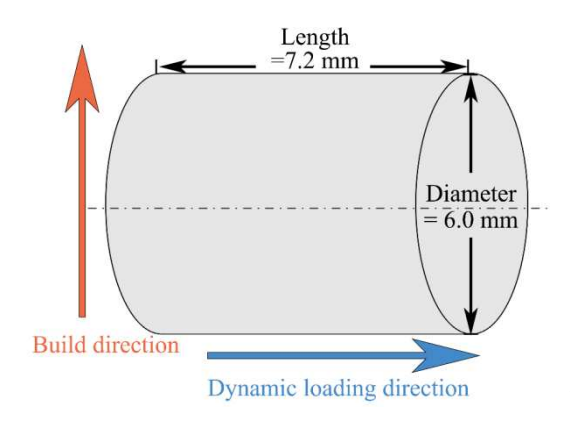


Figure 1 Schematic diagram of cylindrical sample.

To exclude the influence of oxygen on the experiment, before annealing, the specimens were placed in test tubes, washed three times with argon and then sealed. Making sure that the specimens have little exposure to oxygen at high temperatures. Annealing uses the DZSX2-10-12NP (Yun Yue, P. R. China) box type resistance furnace. Four annealing temperatures (700 °C, 750 °C, 800 °C, and 850 °C) were selected and the annealing time is 8 hours. The specimens annealed at 700 °C, 750 °C, 800 °C, and 850 °C are labeled as A700, A750, A800, and A850, respectively, and the specimen ID of the unannealed specimens are As-built. In addition, in the dynamic mechanical properties test, numbers are used to distinguish specific specimen, such as A700-1 and A700-2, which are two specimens. They are both annealed at 700 °C, and the dynamic mechanical properties are tested independently.

The dynamic compression testing performed by the split-Hopkinson pressure bar. The average strain rates in a range of 1500 s⁻¹ - 1600 s⁻¹ were selected. Also, all tests were performed at room temperature (about 298 K). Integrating the true stress-strain curve of dynamic compression, and the average energy absorbed per unit volume in the deformable body can be calculated. This value is named the impact energy. The

maximum stress in the stress-strain curve is called as the ultimate compressive strength. Each specimen information, including the annealing temperature, original size, average strain rate and the bullet velocity of SHPB, are shown in Table 1. The micromechanical properties were examined by nanoindentation. The equipment used was the Nanotest Alpha nano-indenter (Micro Materials, Britain), the loading speed was set to 5 mN·s⁻¹ and the maximum load is 100 mN.

The metallography was observed by a POLYVER-MET optical microscope (Leica, Germany); and the erosion fluid used is a hydrochloric acid: nitric acid: water=15:10:1. The means of microstructure observations include the FEI Quanta-200 scanning electron microscope (SEM) (FEI, Netherlands) and the Tecnai F20 transmission electron microscope (TEM) (FEI, U.S.A.). Use an Image Pro Plus 6.0 (IPP) image analysis software to statistically analyze the and width of the molten pool of as-built specimen and calculate the volume fraction and size of the σ-phase in the annealed SLM-NiCrFeCoMo_{0.2} HEA. X-ray diffraction (XRD) was employed to analyze the phase composition in the sample. The used equipment was the Empyren diffraction instrument (PANalytical, Netherlands) with an incident of the Cu-Kα radiation, the scanning angle was set from 20° to 100°, and the scanning speed was 5 °/min.

The SANS measurement was conducted at China Spallation Neutron Source (CSNS, Dongguan, China). During the experiment, the diameter of specimen aperture was 8 mm. The selected incident neutrons wavelength is 1–10 Å, which can cover a wide Q range from 0.005 Å⁻¹ to 0.60 Å⁻¹. Each specimen was tested for 60 min,

ensuring that sufficient data could be collected. The scattering data were set to absolute unit after normalization, background subtraction and correction with transmission and standard sample calibration. In addition, SasView5.0.5 software is used to analyze the SANS data.

Table 1 The original size and dynamic mechanical properties test conditions of each specimen

Specimen	Annealed	Height	Diameter	Bullet	Average strain
ID	temperature (°C)	(mm)	(mm)	speed (m/s)	rates (s ⁻¹)
As-built	_	7.2	6.0	20.44	1520
A700-1	700			20.49	1570
A700-2				20.17	1500
A750-1	750			20.62	1510
A750-2				20.57	1540
A800-1	800			20.60	1530
A800-2				20.70	1540
A850-1	850			20.72	1580
A850-2				20.95	1600

3. Results

The dynamic mechanical properties of all specimens are shown in Figure 2, which include the true stress-strain curves, average impact energy and ultimate compressive strength. Figures 2(a) and (b) are the true stress-strain curves of different specimens

and compared with the as-build specimen. After similar impacts, all annealed specimens were less deformed than the as-built specimen, and the yield strength increased after annealing. Figure 2(c) is the histogram of the impact energy and ultimate compressive strength. When the annealing temperature did not exceed 800 °C, the two indexes increased with the increase of the annealing temperature, while both showed a downward trend when the annealing temperature reached 850 °C. Compared with the as-built specimen, the impact energy of all annealed specimens is lower, and the maximum compressive strength (MCS) of the A850 specimens reduced to a level close to the as-built specimen. In detail, the impact energy and MCS of the A800 specimens are 217.45 MJ·m⁻³ and 1970 MPa, respectively. The impact energy of A700, A750, A800 and A850 specimens are 94.4 %, 94.7 %, 96.0 %, 92.4 % of those of the as-built specimen, respectively. The MCS of A700, A750, A800 and A850 specimens are 101.2 %, 105.6 %, 108.3 % and 100.3 % of those of the as-built samples, respectively, and the A800 specimen is the highest among them. In Figure 2(d), the impact energy of the A800 specimen is compared with that of some other materials at similar strain rates, includes powder-metallurgy NiCrFeCoMo_{0.2} HEA, powder-metallurgy NiCrFeCoMn HEA [21], powder-metallurgy (NiCrFeCoA_{10.5})_{0.95}Mo_{0.025}C_{0.025}HEA [22], as-cast NiCrFeCoMn HEA [23], forging NiCrFeCoMn HEA [23], as-build SLM-316L stainless steel [24], laser powder bed fusion (LPBF) maraging steel [25] and heattreated SLM-316L stainless steel. The A800 exhibits high impact energy and it can absorb and consume more energy in the process of bearing impact.

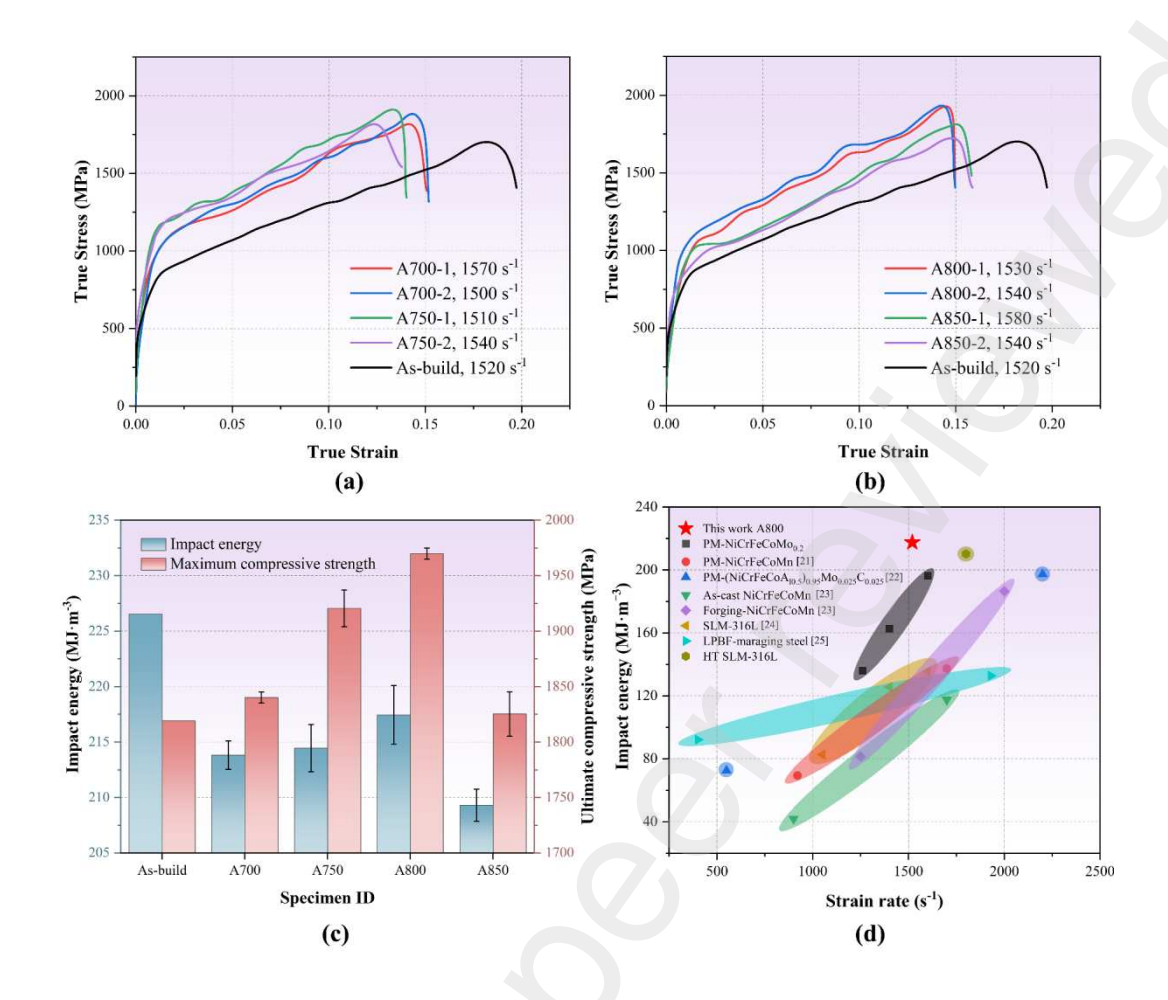


Figure 2 Dynamic mechanical properties. (a) True stress-true strain curves of A700, A750, and asbuild, (b) True stress-true strain curves of A800, A850, and as-build, (c) Comparison of the average impact energy and ultimate compressive strength of each group, (d) Comparison of impact energy between A800 and other materials [21-25].

Figure 3 shows the XRD results, the matrix is a single-phase FCC structure and the diffraction peak of the σ -phase appears in the annealed specimens. The diffraction peak intensities of the σ -phase are stronger in the A750 and A800 specimens, weaker in the A850 specimen, and barely observable in the As-built and A700 specimens. This trend is close to the experimental results of dynamic mechanical properties, indicating that there is a correlation between the content of the σ -phase and the dynamic

mechanical properties.

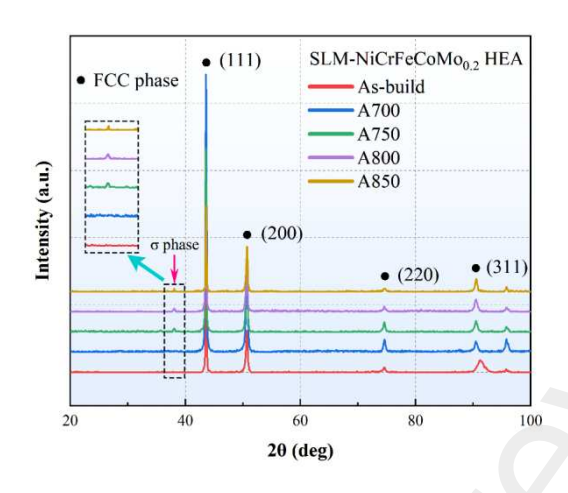


Figure 3 XRD diffractograms of all specimens.

The OM and SEM images of A700, A750, A800, A850 specimens are displayed in Figure 4. The building direction of OM images has marked and adjusted all photos to the same direction. The OM images of A700 and A750 specimens show that, their grain boundaries became recognizable and the molten pool boundaries become blurred. Until the heat treatment temperature reaches 800 °C, the molten pool boundary disappears, but traces at the original molten pool boundary can still be observed. Statistics on the size of the molten pool refer to the molten pool that can be resolved in the optical picture of the as-build specimen. The average depth and width of the molten pool were calculated in planes parallel to and perpendicular to the build direction, respectively. The statistical results show that the depth of molten pool is about $81.1 \pm 5.2 \,\mu m$ and the width is about $94.2 \pm 5.4 \,\mu m$.

The SEM images of different temperatures-annealed specimens. In the image of the A700 specimen, the second phase can hardly be observed. In the SEM image of the A800 specimen, the particles of the second phase continue to grow, and the second

phase inside the molten pool is needle-like, while the second phase along the original molten pool boundary is massive. Compared with the A800 specimen, in the A850 specimen the particle morphology of the second phase remained similar, while the size of the σ precipitates in the molten pool and at the grain boundary decreased, the particles at the original molten pool boundary were growing.

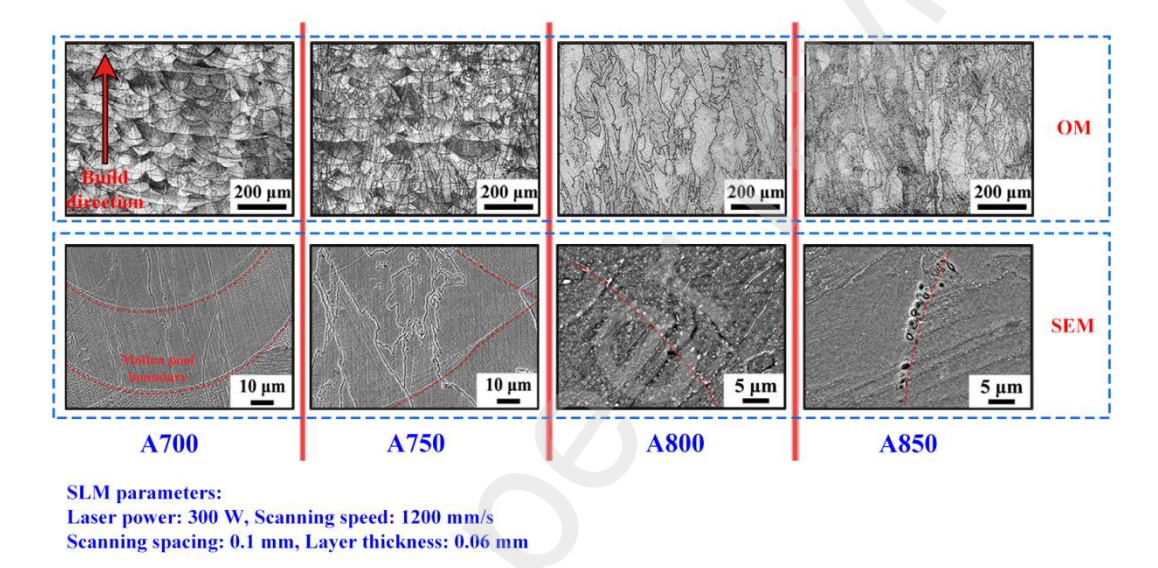


Figure 4 OM and SEM images of A700, A750, A800, A850 specimens.

The changes in mechanical properties of the molten pool boundary after annealing were detected by the nanoindentation experiments. Since the indentation position needs to be located on the molten pool boundary, the A700 specimen was selected for the experiment. Figure 5(a) shows the SEM photos of three nanoindentation points, which are called point a, b, and c, respectively. Among them, point b is located just on the molten pool boundary, points a and c are in a molten pool, located on the cellular crystals with different orientations. Figure 5(b) shows the load-displacement curves corresponding to the three points in Figure 5(a), and the statistical results of hardness values include other nanoindentation points located at the molten pool boundary and

inside. The statistical results show that in the SLM-NiCrFeCoMo_{0.2} HEA annealed at 700 °C, although the sub-grain structure may affect the hardness value, the average hardness at the molten pool boundary is higher than that inside the molten pool.

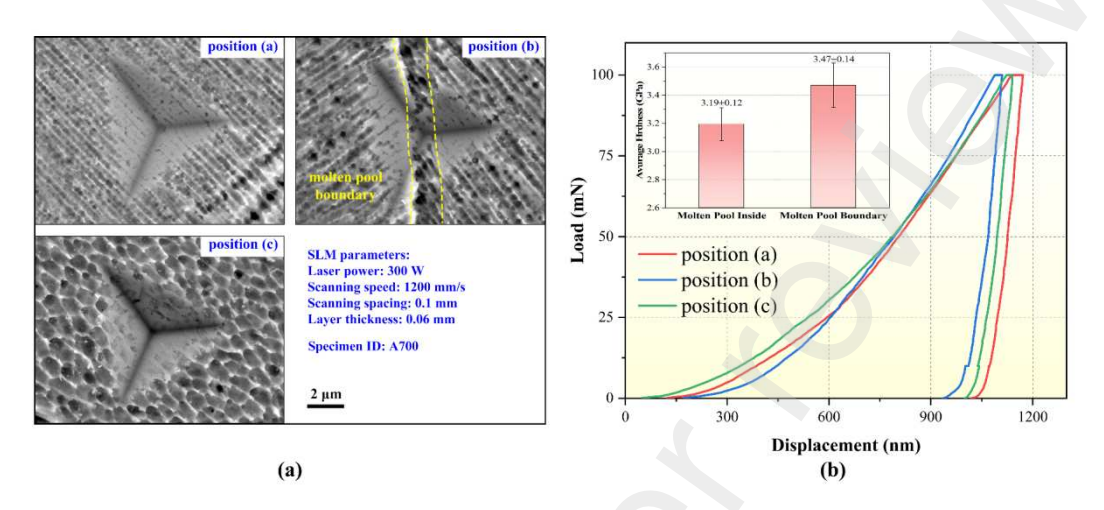


Figure 5 Results of Nanoindentation experiments, (a) SEM photos of the indentations, (b) load-

displacement curves and statistical chart of hardness values.

Figure 6 shows the TEM observation images of the molten pool boundary and σ precipitates. Figure 6(a) is the image of the as-built specimen, there are granular σ precipitates present near the molten pool boundary. The average diameter of these σ precipitates is about 53 nm. Figure 6(b) is the TEM image of the A700 specimen, the σ precipitates was still only observed near the molten pool boundary, and the average size is about 92 nm. This trend indicates that the condition for the growth has been satisfied at this temperature, but no new second particles are generated. Figures 6(c) and (d) are the results of observing the A800 specimen. From Figure 6(c), there are two different forms of σ precipitates. Most of the particles are in the form of strips, and others are larger particles. The strip σ precipitates are coming from the matrix, while the larger blocky σ precipitates may grow from the existing granular particles. The average width

and length of the strip σ precipitates are about 83 nm and 290 nm respectively, and the average size of blocky σ precipitates is about 370 nm. The energy dispersive spectrometer results of the A800 specimen are presented in Figure 6 (d). Ni, Cr, Fe, Co elements are uniformly distributed in the matrix, and Mo elements have enrichment in the σ -phase particles.

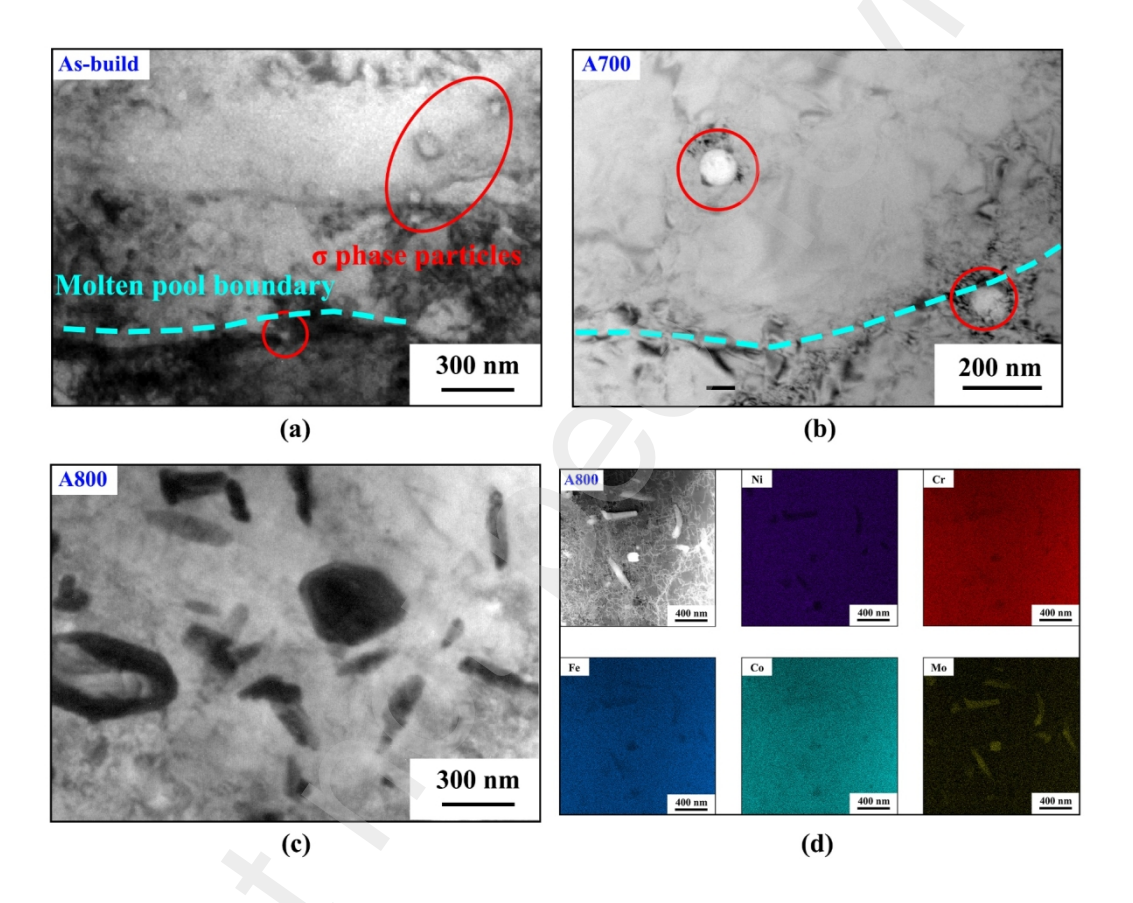


Figure 6 TEM characterization results, (a) As-build, (b) A700, (c) A800, (d) element distribution map of A800.

Therefore, the A800 specimen has a higher ultimate compressive strength. In all annealed specimens than the SLM-NiCrFeCoMo_{0.2} annealed at other temperatures, the ultimate compressive strength and impact energy show the same trend. They rise first with the annealing temperature and drop rapidly after exceeding 800 °C. The results of

nano indentation indicate that after annealing, some defects unfavorable to mechanical properties in the molten pool boundary have disappeared, and the influence of second phase relative hardness gradually dominates, resulting in the hardness value near the boundary exceeding that inside the molten pool. In addition, microscopic observations of the molten pool boundary and precipitates found that the precipitates in the as-build. In the microscopic observation of the molten pool boundary, almost no additional σ precipitates are found in the A700 specimen, while the number and size of precipitates in the A800 specimen have increased.

4. Discussion

In the process of material change, some the microstructure has an effect on the newly formed microstructure, which is called microstructural inheritance [26]. The molten pool structure is a characteristic microstructure of AM products [27]. The molten pool boundary is formed due to remelting and rapid cooling, and many dislocations, grain boundaries, defects are concentrated in the boundary [28, 29], it also provides conditions for the formation of micron-scale gradient structure. In the process of SLM, the segregation of Mo element and second phase particles can be formed at these locations because the temperature of molten pool boundary is conducive to the preferential nucleation of the refractory Mo element. As a result, in the as-build NiCrFeCoMo_{0.2} HEA, although second phase particles can be observed nanoindentation hardness at the molten pool boundary is still lower than that in the molten pool central [30]. After the micron-scale gradient structure design, the

nanoindentation hardness at the molten pool boundary is higher than that at the inner part of the molten pool, indicating that the defects at the boundary disappear and the influence of the second phase particles is more prominent. The molten pool boundary and σ precipitates of the SLM-NiCrFeCoMo_{0.2} HEA have changed in annealing, and this effect on the microstructure is reflected in the dynamic mechanical properties. In the dynamic compression process, these defects and micropores existing in the molten pool boundary are not easy to form cracks, and the as-built SLM-NiCrFeCoMo_{0.2} HEA can absorb more impact energy, which may also be related to these defects.

The volume fraction of σ precipitation in the SLM-NiCrFeCoMo_{0.2} HEA, the specimens were tested using the small angle neutron scattering technique. Figure 7(a) shows the SANS test results. The A800 specimen has the highest scattering intensity, which is consistent with that observed in SEM images. To calculate the volume fraction of σ precipitates, an elliptical particle model is used to fit the SANS data obtained. In this model, the scattering intensity can be described by the following formula [31]:

$$I(q) = \frac{scale}{V} F^{2}(Q) + background \#(1)$$

$$F(Q) = \Delta \rho \cdot V \frac{3(sinqr - qr \cdot cosqr)}{qr^{3}} \#(2)$$

$$r = (R_{e}^{2} + R_{p}^{2})^{1/2} \#(3)$$

$$V = \frac{4}{3} \cdot \pi R_{p} R_{e}^{2} \#(4)$$

where I(q) is the scattering intensity and V is the volume of the ellipsoid, R_p and R_e are the polar radius and equatorial radius perpendicular to the rotational axis of the ellipsoid, respectively. $\Delta \rho$ is the scattering length density difference between the

scatterer and the solvent. The calculated σ precipitation volume fraction is shown in Figure 7 (b). In order to interpret the design of micron-scale gradient structure in SLM-HEA, the molten pool boundary influence area was defined for the A750, A800 and A850 specimens, and shown in Figure 7 (c). different with the molten pool central, σ precipitates of larger particles exist in this area. For distinguish the characteristics of σ precipitation in different parts, the statistical method of its size is carried out in SEM images, and the results are shown in Figure 7 (d).

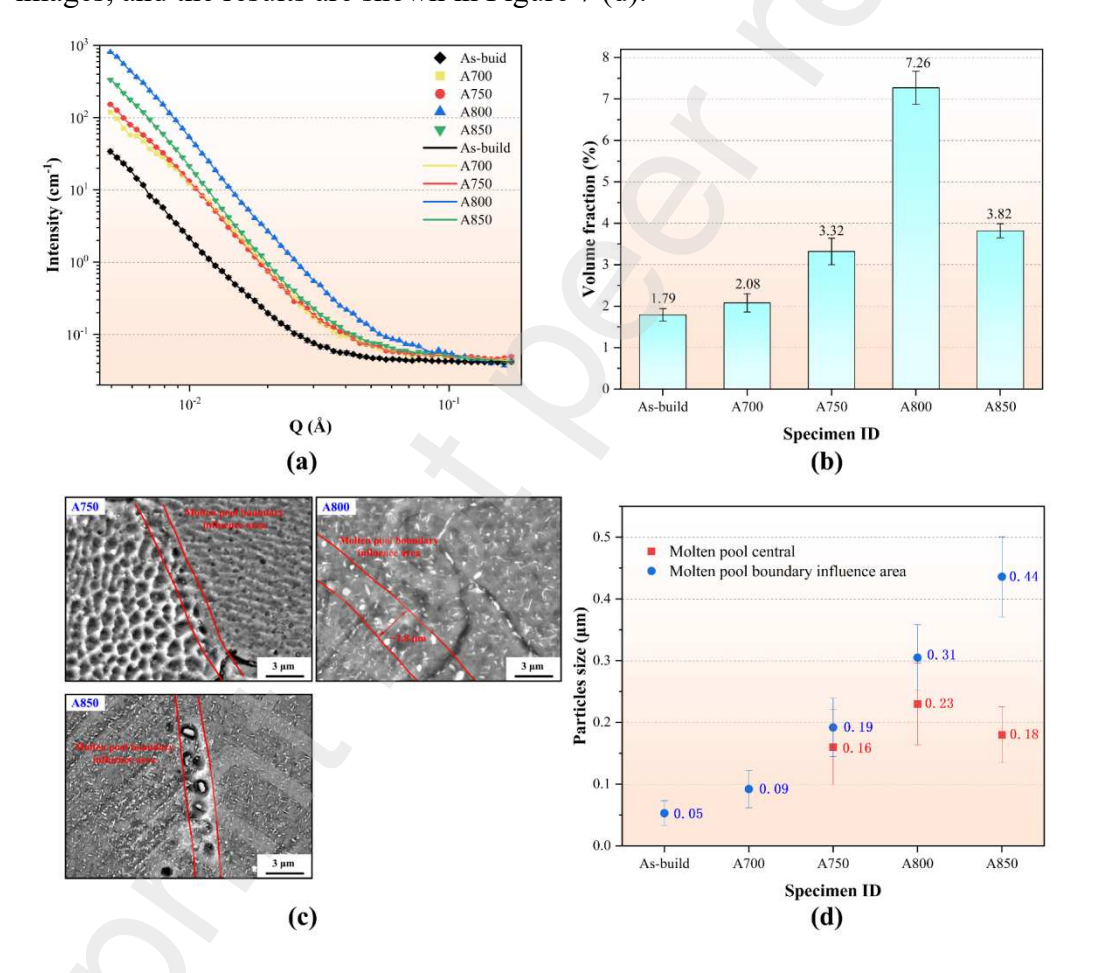


Figure 7 The SANS experiment results were calculated by σ precipitation size. (a) SANS experiment results, (b) σ precipitation volume fraction, (c)molten pool boundary influence area in the A750, A800 and A850 specimens, (d) statistical results of σ precipitates size

The difference between the σ precipitates at the original molten pool boundary and

inside may be caused by the concentration of the Mo element and the small size of σ precipitates inherent in the as-build SLM-NiCrFeCoMo_{0.2} HEA molten pool boundary.

Due to the different characteristics of the second phase generated at the original molten pool boundary and inside after annealing, they should be considered separately in the calculation of the precipitates strengthening. The annealed SLM- NiCrFeCoMo_{0.2} HEA can be divided into two regions: near the original molten pool boundary area and the molten pool inside. The second phase reinforcement value can be expressed by the rule of mixture as [32]:

$$\sigma_{sp} = k\sigma_{sp(boundary)} + (1 - k)\sigma_{sp(inside)} \#(5)$$

where $\sigma_{sp(boundary)}$ and $\sigma_{sp(inside)}$ refer to the precipitates strengthening values near the molten pool boundary and inside respectively.

In the A800 and A850 specimens, the area affected by the original molten pool boundary is a band with a width (a) of about 2.8 µm. The shape of the molten pool boundary can be regarded as a semi-ellipse, and the volume fraction (k) of the molten pool boundary affected area in the sample can be estimated by the width (W) and depth (D) of the molten pool. The expression is [30]:

$$k = \frac{2 \times a}{DW} \left[\pi \frac{1}{2} W + 2 \left(D - \frac{1}{2} W \right) \right] \#(6)$$

It can be considered that the molten pool sizes of these specimens are the same, so k=0.16 is calculated.

The σ precipitates are incoherent with the FCC matrix, and the precipitates strengthening Orowan bypass mechanism predominates. The equation for the intensity

increment is presented as follows [33]:

$$\sigma_{\text{orowan}} = M \times \frac{0.4Gb}{\pi\sqrt{1 - v}} \times \frac{\ln{(\frac{2\sqrt{2/3}r}{b})}}{L} \#(7)$$

$$L = \sqrt{\frac{2}{3}r\sqrt{\frac{\pi}{4}f} - 1} \#(8)$$

where, M = 3.06, b is the Burgers vector; v is the Poisson's ratio; G is the shear-modulus of the matrix; v is the average size of precipitates; v is the inter-precipitate spacing and v is the volume fraction of precipitates. Also, take v = 0.26 [34], v GPa [35], and the Burgers vector is 0.255 nm [8].

The size and volume fraction of σ precipitates for calculating the precipitates strengthening of A750, A800, and A850 specimens are from Figure 7. In as-build and A700 specimens, no σ precipitates observed inside the molten pool, and the size of the σ precipitates near the molten pool boundary was obtained by TEM images, which is also referred to the previous work [30]. The contribution of the precipitates strengthening to the strength of these specimens is shown in Figure 8.

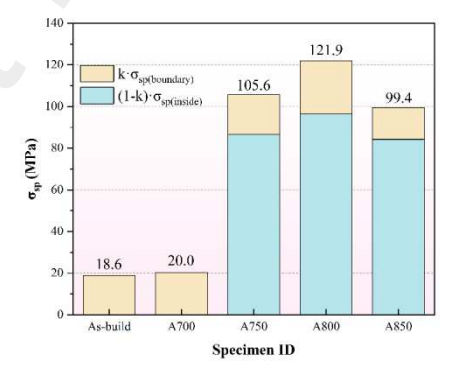


Figure 8 Strength contribution of σ precipitates at the molten pool boundary and inside of each group.

The calculated values of the precipitates strengthening have a correlation with the

dynamic mechanical properties. As as-build and A700 specimens only observed a small number of second phase particles at the molten pool boundary, the precipitates strengthening values of the two specimens were calculated to be close to the ultimate compressive strength measured by the experiment. The strength difference between the A700 and A750 specimens is larger than the experimental data, which may be due to the decrease of the dislocation density and the increase of the grain size during annealing at 750 °C [36]. The A800 specimen has the best dynamic mechanical properties, in which the precipitates strengthening plays an important role, the A800 specimen is annealed at a higher temperature and produce less σ precipitates, and the overall strength also decreases.

5. Conclusions

For the SLM-NiCrFeCoMo_{0.2} HEA, the micron scale gradient structure provides excellent dynamic mechanical properties for this material. Although the impact energy decreased slightly due to the disappearance of microscopic defects, the A800 specimen still maintains the impact energy of 217.45 MJ·m⁻³ at the strain rate of 1520s⁻¹, and the dynamic UCS reaches 1,970 MPa.

The annealed SLM-NiCrFeCoMo $_{0.2}$ HEA consists of an FCC matrix and σ -phase, and the σ -phase has the strongest diffraction peak in the A800 specimen. In addition, the molten pool boundary in the A800 specimen has almost disappeared, but the formation of more σ precipitates in these locations makes the original molten pool boundary discernible.

The average hardness of the specimen annealed at 700 °C near the molten pool boundary is about 8.78% higher than that inside the molten pool. However, in the asbuild specimen, the hardness inside the molten pool is higher. This trend may be because annealing eliminates the defects in the boundary and makes the existing σ precipitates grow larger, but there is no σ precipitates in the molten pool central.

The content of the σ -phase in the SLM-NiCrFeCoMo_{0.2} HEA reaches the peak value after annealing at 800 °C, which is similar to the change of dynamic mechanical properties. Moreover, the microstructural inheritance of molten pool boundary in annealing is due to the Mo segregation at the molten pool boundary in the SLM process, there are more σ precipitates near the original molten pool boundary than the molten pool inside thus forming a structure with σ precipitation gradient distribution.

Declaration of interest statement

The authors declare that they have no known competing financial interests or personal relationships that could have appeared to influence the work reported in this paper.

Acknowledgments

The present work was financially supported by the National Natural Science Foundation of China (No. 52020105013), and by the State Key Laboratory of Powder Metallurgy (No. 62102172). Prof. Peter Liaw gratefully acknowledges the support of the National Science Foundation (DMR-1611180, 1809640, and 2226508) with program directors, Drs. J. Madison, J. Yang, G. Shiflet, and D. Farkas.

Author contributions

Conceptualization, B. W., and B. L.; methodology, Y. H., W. L., Q. W., and H. C.; validation, B. W. and B. L.; formal analysis, B. W., Y. H., and B. L.; investigation, Y. H., W. L., Q. W., and H. C.; resources, B. L.; data curation, Y. H., W. L., H. C., Q.W., and S. W.; writing-original draft preparation, B. W., B. L., and Y. H.; writing-review and editing, B. W., P. L., Y. H., and B. L.; visualization, Y. H.; supervision, B. W., and B. L.; project administration, B. W. and B. L.; funding acquisition, B. W., and B. L..

References

[1] Zhang, Y., Zuo, T.T., Tang, Z., Gao, M.C., Dahmen, K.A., Liaw, P.K., Lu, Z.P. Microstructures and properties of high-entropy alloys. Prog Mater Sci 61, 1-93(2014).

DOI: doi.org/10.1016/j.pmatsci.2013.10.001

[2] Cantor, B. Multicomponent high-entropy Cantor alloys. Prog Mater Sci 120, 100754(2021).

DOI: doi.org/10.1016/j.pmatsci.2020.100754

[3] Moghaddam, A.O., Shaburova, N.A., Samodurova, M.N., Abdollahzadeh, A., Trofimova, E.A. Additive manufacturing of high entropy alloys: A practical review.

J Mater Sci Technol 77(30), 131-162(2021).

DOI: doi.org/10.1016/j.jmst.2020.11.029

[4] Fujieda, T., Chen, M., Shiratori, H., Kuwabara, K., Yamanaka, K., Koizumi, Y., Chiba, A., Watanabe, S. Mechanical and corrosion properties of CoCrFeNiTi-based high-entropy alloy additive manufactured using selective laser melting. Addit Manuf 25, 412-420(2019).

DOI: doi.org/10.1016/j.addma.2018.10.023

[5] Lin, W.C., Chang, Y.J., Hsu, T.H., Gorsse, S., Sund, F., Furuhara, T., Yeh, A.C. Microstructure and tensile property of a precipitation strengthened high entropy alloy processed by selective laser melting and post heat treatment. Addit Manuf 36, 101601(2020).

DOI: doi.org/10.1016/j.addma.2020.101601

[6] Kim, Y.K., Baek, M.S., Yang, S., Lee, K.A. In-situ formed oxide enables extraordinary high-cycle fatigue resistance in additively manufactured CoCrFeMnNi high-entropy alloy. Addit Manuf 38, 101832(2021).

DOI: doi.org/10.1016/j.addma.2020.101832

- [7] Karthik, G.M., Kim, E.S., Sathiyamoorthi, P., Zargaran, A., Jeong, S.G., Xiong, R., Kang, S.H., Cho, J.W., Kim, Delayed, H.S. Deformation-induced martensite transformation and enhanced cryogenic tensile properties in laser additive manufactured 316L austenitic stainless steel. Addit Manuf 47, 102314(2021).

 DOI: doi.org/10.1016/j.addma.2020.102314
- [8] Liu, W.H., Lu, Z.P., He, J.Y., Luan, J.H., Wang, Z.J., Liu, B., Liu, Y., Chen, M.W., Liu, C.T. Ductile CoCrFeNiMo_x high entropy alloys strengthened by hard intermetallic phases. Acta Mater 116, 332-342(2016).
 DOI: doi.org/10.1016/j.actamat.2016.06.063
- [9] Sing, S.L., An, J., Yeong, W.Y., Wiria, F.E. Laser and electron-beam powder-bed additive manufacturing of metallic implants: A review on processes, materials and designs. J. Orthop. Res 34(3), 369-385(2016).
 DOI: doi.org/10.1002/jor.23075
- [10] Zhang, T.L., Huang, Z.H., Yang, T., Kong, H.J., Luan, J.H., Wang, A.D., Kuo, W., Wang, Y.Z., Liu, C.T. In situ design of advanced titanium alloy with concentration modulations by additive manufacturing. Science 374(6566), 478-482(2021).
 DOI: doi.org/10.1126/science.abj3770

[11] Wu, Y.W., Zhao, X.Y., Chen, Q., Yang, C., Jiang, M.G., Liu, C.Y., Jia, Z., Chen, Z.W., Yang, T., Liu, Z.Y. Strengthening and fracture mechanisms of a precipitation hardening high-entropy alloy fabricated by selective laser melting. Virtual Phys Prototy 17(3), 451-467(2022).

DOI: doi.org/10.1080/17452759.2022.2037055

[12] Kim, Y.K. & Lee, K.A. Stabilized sub-grain and nano carbides-driven 1.2 GPa grade ultra-strong CrMnFeCoNi high-entropy alloy additively manufactured by laser powder bed fusion. J Mater Sci Technol 117(1), 8-22(2022).

[13] Park, J.M., Kim, E.S., Kwon. H., Sathiyamoorthi, P., Kim, K.T., Yu, J.H., Kim, H.
S. Effect of heat treatment on microstructural heterogeneity and mechanical properties of 1%C-CoCrFeMnNi alloy fabricated by selective laser melting. Addit Manuf 47, 102283(2021).

DOI: doi.org/10.1016/j.addma.2021.102283

DOI: doi.org/10.1016/j.jmst.2021.12.010

[14] Lin, D.Y., Xu, L.Y., Jing, H.Y., Han, Y.D., Zhao, L., Minami, F. Effects of annealing on the structure and mechanical properties of FeCoCrNi high-entropy alloy fabricated via selective laser melting. Addit Manuf 32, 101058(2020).
DOI: doi.org/10.1016/j.addma.2021.101058

[15] Nandal, V., Sarvesha, R., Singh, S.S., Huang, E-W., Chang, Y.J., Yeh, A.C., Jain, J., Neelakantan, S. Enhanced age hardening effects in FCC based Co_{1.5}CrFeNi_{1.5} high entropy alloys with varying Ti and Al contents. Materialia 13, 100823(2020).

DOI: doi.org/10.1016/j.mtla.2020.100823

[16] Yeh, J.W., Chen, S.K., Lin, S.J., Gan, J.Y., Chin, T.S., Shun, T.T., Tsau, C.H., Chang, S.Y. Nanostructured high-entropy alloys with multiple principal elements:

Novel alloy design concepts and outcomes. Adv Eng Mater 6(5), 299-303(2004).

DOI: doi.org/10.1002/adem.200300567

[17] Liu, L.Y., Zhang, Y., Han, J.H., Wang, X.Y., Jiang, W.Q., Liu, C.T., Zhang, Z.G., Liaw, P.K. Nanoprecipitate-Strengthened High-Entropy Alloys. Adv Sci 8(23), 2100870(2021).

DOI: doi.org/10.1002/advs.202100870

[18] Li, N., Chen, W.T., He, J.Y., Gu, J., Wang, Z.W., Li, Y., Song, M. Dynamic deformation behavior and microstructure evolution of CoCrNiMo_x medium entropy alloys. Mat Sci Eng A 827(19), 142048(2021).

DOI: doi.org/10.1016/j.msea.2021.142048

[19] Zhang, L., Huo, X.F., Wang, A.G., Du, X.H., Zhang, L., Li, W.P., Zou, N.F., Wan, G., Duan, G.S., Wu, B.L. A ductile high entropy alloy strengthened by nano sigma phase. Intermetallics 122, 106813(2020).

DOI: doi.org/10.1016/j.intermet.2020.106813

[20] Bae, J.W., Park, J.M., Moon, J., Choi, W.M., Lee, B.-J., Kim, H.S. Effect of μ-precipitates on the microstructure and mechanical properties of non-equiatomic CoCrFeNiMo medium-entropy alloys. J Alloy Compd 781(15), 75-83(2019).

DOI: doi.org/10.1016/j.jallcom.2018.12.040

[21] Wang, B.F., Huang, X.X., Fu, A., Liu, Y., Liu, B. Serration behavior and microstructure of high entropy alloy CoCrFeMnNi prepared by powder metallurgy. Mat Sci Eng A 726(30), 37-44(2018).
DOI: doi.org/10.1016/j.msea.2018.04.071

[22] Wang, B.F., Wang, C., Liu, B., Zhang, X.Y. Dynamic Mechanical Properties and Microstructure of an (Al_{0.5}CoCrFeNi)_{0.95}Mo_{0.025}C_{0.025} High Entropy Alloy. Entropy 21(12), 1154(2019).

DOI: doi.org/10.3390/e21121154

[23] Liu, R.Y., Yao, X.R., Wang, B.F. Mechanical Properties and Serration Behavior of a NiCrFeCoMn High-Entropy Alloy at High Strain Rates. Materials 13(17), 3722(2020).

DOI: doi.org/10.3390/ma13173722

- [24] Chen, H.Y., Li, W.S., Huang, Y.Y., Xie, Z.H., Zhu, X.B., Liu, B., Wang, B.F..
 Molten pool effect on mechanical properties in a selective laser melting 316 L
 stainless steel at high-velocity deformation. Mater Charact 194, 112409(2020).
 DOI: doi.org/10.1016/j.matchar.2022.112409
- [25] Dehgahi, S., Alaghmandfard, R., Tallon, J., Odeshi, A., Mohammadi, M. Microstructural evolution and high strain rate compressive behavior of as-built and heat-treated additively manufactured maraging steels. Mat Sci Eng A 815(20), 141183(2021).

DOI: doi.org/10.1016/j.msea.2021.141183

- [26] Hu, B. & Luo, H.W. A novel two-step intercritical annealing process to improve mechanical properties of medium Mn steel. Acta Mater 176, 250-263(2019).

 DOI: doi.org/10.1016/j.actamat.2019.07.014
- [27] Fayazfar, H., Salarian, M., Rogalsky, A., Sarker, D., Russo, P., Paserin, V., Toyserkani, E. A critical review of powder-based additive manufacturing of ferrous alloys: Process parameters, microstructure and mechanical properties.
 Mater Design 114(15), 98-128(2018).
- [28] Zhou, R., Liu, Y., Zhou, C.S., Li, S.Q., Wu, W.Q., Song, M., Liu, B., Liang, X.P., Liaw, P.K. Microstructures and mechanical properties of C-containing FeCoCrNi high-entropy alloy fabricated by selective laser melting. Intermetallics 94, 165-171(2018).

DOI: doi.org/10.1016/j.intermet.2018.01.002

DOI: doi.org/10.1016/j.matdes.2018.02.018

- [29] Piglione, A., Dovgyy, B., Liu, C., Gourlay, C.M., Hooper, P.A., Pham, M.S. Printability and microstructure of the CoCrFeMnNi high-entropy alloy fabricated by laser powder bed fusion. Mater Lett 224, 22-25(2018).
 DOI: doi.org/10.1016/j.matlet.2018.04.052
- [30] Huang, Y.Y., Xie, Z.H., Li, W.S., Chen, H.Y., Liu, B., Wang, B.F. Dynamic mechanical properties of the selective laser melting NiCrFeCoMo_{0.2} high entropy alloy and the microstructure of molten pool. J Alloy Compd. 297(15), 167011(2022).

DOI: doi.org/10.1016/j.jallcom.2022.167011

[31] Guo Y., Wei, S.H., Yang, S., Ke, Y.B., Zhang, X.Y., Zhou, K.C. Precipitation Behavior of ω Phase and ω→α Transformation in Near β Ti-5Al-5Mo-5V-1Cr-1Fe Alloy during Aging Process. Metals 11(2), 273(2021).

DOI: doi.org/10.3390/met11020273

[32] Tong, Y., Chen, D., Wang, J., Feng, R., Yang, T., Zhao, C., Zhao, Gao, L.Y., Shinizu W. Y. Outstanding tensile properties of a precipitation-strengthened FeCoNiCrTi_{0.2} high-entropy alloy at room and cryogenic temperatures. Acta Mater. 165, 228-240(2019).

DOI: doi.org/10.1016/j.actamat.2018.11.049

[33] Kim, Y.K., Choe, J., Lee, K.A. Selective laser melted equiatomic CoCrFeMnNi high-entropy alloy: Selective laser melted equiatomic CoCrFeMnNi high-entropy alloy: Microstructure, anisotropic mechanical response, and multiple strengthening mechanism. J Alloy Compd 805(15), 680-691(2019).

DOI: doi.org/10.1016/j.jallcom.2019.07.106

- [34] Park, J.M., Choe, J., Kim, J.G., Bea, J.W., Moon, J., Yang, S., Kim, K.T., Yu, J.H., Kim, H.S. Superior tensile properties of 1%C-CoCrFeMnNi high-entropy alloy additively manufactured by selective laser melting. Mater Res Lett 8(1), 1-7(2020). DOI: doi.org/10.1080/21663831.2019.1638844
- [35] Lin, Q.Y, An, H.X., Liu, H.W., Tang, Q.H, Dai, P.Q., Liao, X.Z. In-situ high-resolution transmission electron microscopy investigation of grain boundary dislocation activities in a nanocrystalline CrMnFeCoNi high-entropy alloy. J Alloy Compd 709, 802-807(2017).

DOI: doi.org/10.1016/j.jallcom.2017.03.194

[36] Hong, Y.J., Zhou, C.S., Zheng, Y.Y., Zhang, L., Zheng, J.Y. The cellular boundary with high density of dislocations governed the strengthening mechanism in selective laser melted 316L stainless steel. Mat Sci Eng A 799(2), 140279(2021).

DOI: doi.org/10.1016/j.msea.2020.140279

Figure Captions

Figure 1 Schematic diagram of cylindrical sample.

Figure 2 Dynamic mechanical properties. (a) True stress-true strain curves of A700, A750, and as-build, (b) True stress-true strain curves of A800, A850, and as-build, (c) Comparison of the average impact energy and ultimate compressive strength of each group, (d) Comparison of impact energy between A800 and other materials [21-25]. Figure 3. XRD diffractograms of all specimens.

Figure 4 OM and SEM images of A700, A750, A800, A850 specimens.

Figure 5 Results of Nanoindentation experiments, (a) SEM photos of the indentations, (b) load-displacement curves and statistical chart of hardness values.

Figure 6 TEM characterization results, (a) As-build, (b) A700, (c) A800, (d) element distribution map of A800.

Figure 7 The SANS experiment results were calculated by σ precipitation size. (a) SANS experiment results, (b) σ precipitation volume fraction, (c)molten pool boundary influence area in the A800 specimen, (d) statistical results of σ precipitates size Figure 8 Strength contribution of σ precipitates at the molten pool boundary and inside of each group.

Table Captions

Table 1. The original size and dynamic mechanical properties test conditions of each specimen